Trends in the CERES Dataset, 2000–13: The Effects of Sea Ice and Jet Shifts and Comparison to Climate Models

DENNIS L. HARTMANN AND PAULO CEPPI

Department of Atmospheric Sciences, University of Washington, Seattle, Washington

(Manuscript received 12 July 2013, in final form 7 November 2013)

ABSTRACT

The Clouds and the Earth's Radiant Energy System (CERES) observations of global top-of-atmosphere radiative energy fluxes for the period March 2000–February 2013 are examined for robust trends and variability. The trend in Arctic ice is clearly evident in the time series of reflected shortwave radiation, which closely follows the record of ice extent. The data indicate that, for every 10^6 km^2 decrease in September sea ice extent, annual-mean absorbed solar radiation averaged over 75°–90°N increases by 2.5 W m^{-2}, or about 6 W m^{-2} between 2000 and 2012. CMIP5 models generally show a much smaller change in sea ice extent over the 1970–2012 period, but the relationship of sea ice extent to reflected shortwave is in good agreement with recent observations. Another robust trend during this period is an increase in reflected shortwave radiation in the zonal belt from 45° to 65°S. This trend is mostly related to increases in sea ice concentrations in the Southern Ocean and less directly related to cloudiness trends associated with the annular variability of the Southern Hemisphere. Models from phase 5 of the Coupled Model Intercomparison Project (CMIP5) produce a scaling of cloud reflection to zonal wind increase that is similar to trend observations in regions separated from the direct effects of sea ice. Atmospheric Model Intercomparison Project (AMIP) model responses over the Southern Ocean are not consistent with each other or with the observed shortwave trends in regions removed from the direct effect of sea ice.

1. Introduction

The Clouds and the Earth's Radiant Energy System (CERES) experiment makes precise measurements of Earth's broadband solar and longwave irradiance (Loeb et al. 2012a; Wielicki et al. 1996). The dataset is unprecedented in its consistency and accuracy (Loeb et al. 2012b). Although a 13-yr record is short for climate analysis, the dataset deserves a careful look to see what it can tell us about connections within the climate system, even though the changes we observe on such short time scales are likely heavily influenced by natural variability. Two things of interest that the dataset should be able to measure are the sensitivity of the energy balance to changing polar ice and the relationship of cloud albedo to the position of the extratropical jet in the Southern Hemisphere. We will begin by looking for statistically significant linear trends in zonal–annual means of the data and will then attempt to make quantitative estimates of the sensitivity of reflected solar radiation to sea ice extent and the southern annular mode and compare with climate model simulations.

2. Data and methods

The CERES data used are the monthly-mean Energy Balanced and Filled (EBAF) version 2.7 data for the period of March 2000 through February 2013, a period of 13 yr. The time series of sea ice extent in September was obtained from the National Snow and Ice Data Center (Fetterer et al. 2009). We also make use of the merged Hadley Centre–National Oceanic and Atmospheric Administration (NOAA) optimum interpolated (OI) sea surface temperature (SST) and sea ice concentration dataset (Hurrell et al. 2008; Rayner et al. 2003). These data are also boundary conditions for the Atmospheric Model Intercomparison Project (AMIP) simulations we will use. The sea ice concentration measurements are based primarily on microwave satellite measurements and should not be sensitive to the presence of clouds of water or ice. The annular variability is characterized by the upper tropospheric zonal wind averaged over

Corresponding author address: Dennis L. Hartmann, Department of Atmospheric Sciences, University of Washington, Box 351640, Seattle, WA 98195-1640.
E-mail: dennis@atmos.washington.edu

DOI: 10.1175/JCLI-D-13-00411.1

© 2014 American Meteorological Society

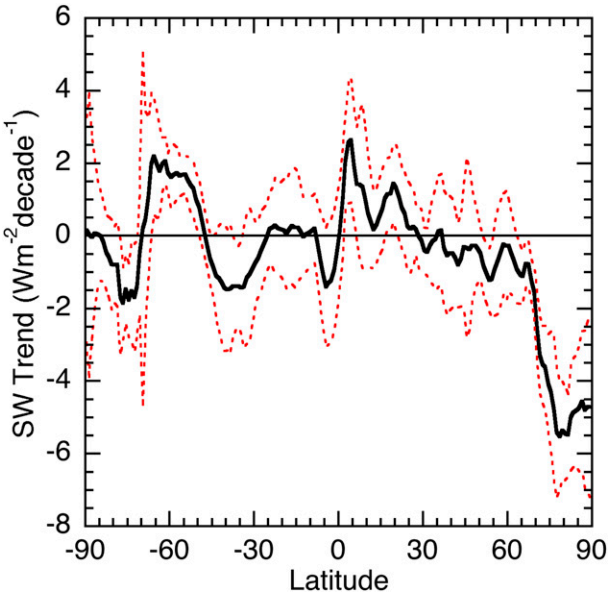


FIG. 1. Trend in reflected shortwave computed from annual-mean data and plotted as a function of latitude. The solid line shows the linear trend difference over the period 2000–12 for the zonal- and annual-mean reflected shortwave. The dashed lines show the 5% and 95% confidence levels.

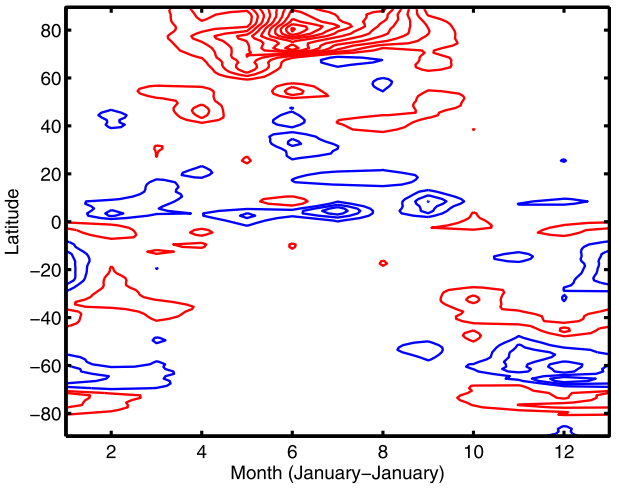


FIG. 2. Trend in reflected shortwave for 2000–12 computed from monthly data and plotted as a function of latitude and month. Contour interval is $2\,\mathrm{W\,m^{-2}\,decade^{-1}}$ and the zero contour is omitted. Red contours indicate a reduction in reflected SW and blue contours indicate an increase.

45°–65°S, which is well correlated with other indices of annular variability. Three-dimensional monthly-mean meteorological fields were obtained from both the National Centers for Environmental Prediction–National Center for Atmospheric Research (NCEP–NCAR) reanalysis dataset (Kalnay et al. 1996) and the European Centre for Medium-Range Weather Forecasts (ECMWF) Interim Re-Analysis (ERA-Interim) dataset (Dee et al. 2011).

To compare the observed changes with climate models, we analyze the output of 34 models from phase 5 of the Coupled Model Intercomparison Project (CMIP5) (Taylor et al. 2012), listed in the appendix. We combine the historical and representative concentration pathway (RCP) 8.5 integrations to yield time series for the period March 1970–February 2013. We use this longer period from the models so that the trend magnitude is more robust and more comparable in size to the trend in the data. The variables used are sea ice area fraction, outgoing top-of-atmosphere shortwave radiation, and zonal wind, and the data are averaged annually. For each model, we use only the first ensemble member ("r1i1p1"). In addition, we use AMIP runs from the CMIP5 archive.

To assess linear trends we use the methodology described in Santer et al. (2008), which uses the theory described in Sveshnikov (1968) and the formulas from Bretherton et al. (1999) to estimate the degrees of freedom of an autoregressive-1 (AR-1) process. Uncertainties are plotted for 5% and 95% confidence levels so that, if an uncertainty bound is above (below) zero, the chance that the trend is not positive (negative) is less than 5%. Lines appearing in scatterplots were determined by principal component analysis rather than ordinary least squares.

3. Results

a. *Global trends*

Figure 1 shows the linear trend of the annually and zonally averaged reflected shortwave (SW) as a function of latitude, along with the 5% and 95% confidence intervals on the trend. The year is defined as the average of March through February so that 13 12-month means can be computed. Although trends are computed from a 12-yr difference, they are reported as change per decade. The most robustly significant changes are a decreasing trend over the Arctic and an increasing trend over the Southern Ocean from 45° to 65°S. The seasonal and latitudinal distributions of these changes are illustrated in Fig. 2, which shows a contour plot of the linear trend in monthly-mean SW over 2000–12 as a function of latitude and month. As expected, the shortwave trends in the Arctic occur primarily in the spring and summer seasons. The Arctic trend dips down to 60°N in May, indicating a significant contribution from earlier snowmelt in land areas of the Arctic (Derksen and Brown 2012).

The spatial distribution of the trends in annual-mean SW is shown in Fig. 3. Three features are of interest. The negative trends in Arctic SW are greatest in the Canadian and Siberian sectors but span the Arctic Ocean. These changes are contributed mostly by the summer half year in middle and high latitudes. Over the

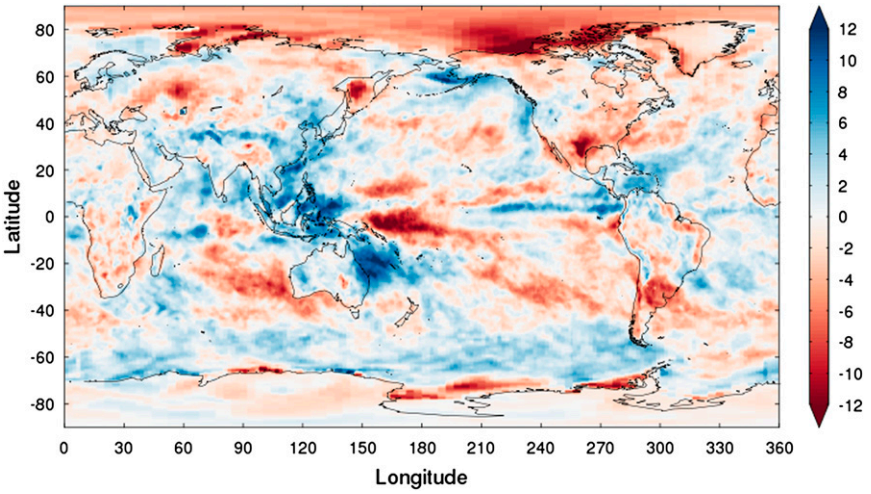


FIG. 3. Linear trend of CERES annual-mean reflected shortwave computed for each 1° × 1° region of the globe ($W\,m^{-2}\,decade^{-1}$).

Southern Ocean the reflected shortwave increases modestly over a broad region between 45° and 65°S in the Indian and Pacific Ocean sectors. The trends at many of these points are statistically significant, and no points have statistically significant negative trends. The Southern Ocean trend is visible in every season as well, so it is quite robust during this period. Some trends toward less reflection can be seen along the coast of Antarctica and in the Ross Sea that are related to declines in sea ice there in the summer season. The effects of sea ice concentration trends in the Southern Ocean will be discussed more fully later.

The spatial structure of the trend in annual-mean reflected shortwave in Fig. 3 strongly suggests a trend toward La Niña conditions over this period, as indicated by the decreasing reflection near the dateline and the increased reflection west of the dateline and from an analysis of sea surface temperature (not shown). The La Niña trend also accounts for the upward trend in zonal-mean SW between the equator and 10°N in Fig. 1, since as equatorial east Pacific SST cools during La Niña the ITCZ is more concentrated north of the equator there. A northward movement of the ITCZ would be consistent with the greater absorption of energy in the Northern Hemisphere accompanying the polar ice melt following the reasoning of Chiang and Bitz (2005) and Frierson and Hwang (2012), but the integrated effect of this increased Arctic energy intake seems too small to be important compared to the influence of ENSO during the period of the CERES data.

b. *Arctic trends and sea ice*

The trend over the Arctic is clearly related to the decline in sea ice extent and associated snow cover during this period. The climate feedbacks associated with observed changes in surface ice have been recently assessed by Flanner et al. (2011). The left panel of Fig. 4 shows the September sea ice extent and the annual-mean SW averaged over the area poleward of 75°N as a function of year. The right panel shows a scatterplot of the same two quantities. From the linear fit in Fig. 4, we infer that, for each million square kilometers ($10^6\,km^2$) of sea ice extent removed, the SW at the top of the atmosphere averaged poleward of 75°N decreases by about $2.5\,W\,m^{-2}$. That translates into an albedo change of about 0.013 $(10^6\,km^2)^{-1}$. These are annual averages, and the changes are much larger in summer. The polar cap albedo declined by about 0.034 or about 6% between 2000 and 2012, while the sea ice extent in September declined about 40%. The change in mean solar absorption poleward of 75°N over this period is about $6\,W\,m^{-2}$ for the annual mean and $20\,W\,m^{-2}$ for the June through August average. From Fig. 4 it is clear that year-to-year variations in SW over the pole are closely related to sea ice extent. Changes in clouds may also have an influence, primarily by screening the surface albedo changes from affecting the top-of-atmosphere budget as much as they might, but there may also be changes in cloudiness associated with the sea ice change. We have not attempted to assess cloud changes, except to note that the observed top-of-atmosphere response to sea ice extent is reasonably well simulated by models (Kay and Gettelman 2009). CERES clear-sky estimates suggest that about half of the surface albedo decrease because ice melt is screened by clouds and thereby not apparent at the top of the atmosphere (N. Loeb 2013, personal communication).

Figure 5 shows the same data as Fig. 4, except for the multimodel mean of the CMIP5 models. The downward

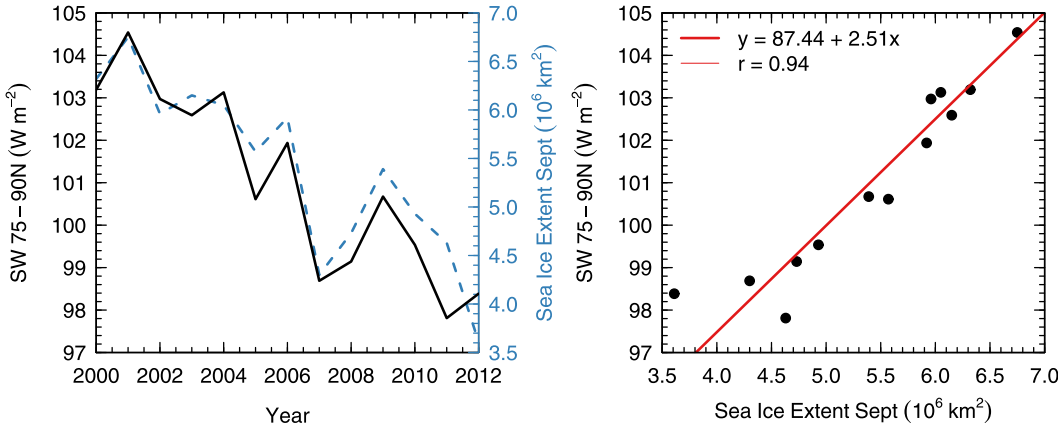


FIG. 4. (left) Annual-mean CERES reflected shortwave area averaged from 75° to 90°N for each (March–February average) vs the sea ice extent in September of the same year. (right) Scatterplot of annual-mean CERES shortwave reflected averaged over the area poleward of 75°N vs Arctic sea ice extent in September for 2000–12.

trend in sea ice is much smaller in the multimodel mean than in observations (see also Stroeve et al. 2012; Wang and Overland 2012), but the relationship of changes in reflected solar radiation to changes in sea ice extent is similar. The model data are more scattered in part because the changes are so much smaller, but the ratio of sea ice extent decline to reflected radiation decline of about 2 W m^{-2} (10^6 km^2)$^{-1}$ is not too dissimilar from that of the observations, indicating that cloud overlap and other influences that would affect the albedo change are not grossly different between the models and observations.

Figure 6 shows the scatterplot of trends in sea ice extent and reflected shortwave for 34 models and for the observations. The slope of the fit to the model data is about 2.3 W m^{-2} (10^6 km^2)$^{-1}$, in good agreement with Fig. 5. The models and the data are on the same line, but the observed trends are larger than all of the models and much larger than the multimodel mean, as previously shown.

c. *Southern Ocean trends and annular variability*

The change in SW over the Southern Ocean is likely to be associated with changes in the position or strength of the extratropical jet, since the cloud reflectivity increases poleward of 45°S and decreases equatorward of 45°S. The mean jet position is at about 52°S (e.g., Barnes and Hartmann 2010). Bender et al. (2012) did an exhaustive analysis of International Satellite Cloud Climatology Project (ISCCP) data and concluded that the clouds have shifted poleward during the period 1983–2008. Climate models also show a similar shift with global warming (Kushner et al. 2001; Yin 2005), with negative cloud feedback poleward of about 45°S and positive feedback equatorward of it (Zelinka and Hartmann 2012), which may be related to a poleward jet shift as well as thermodynamic factors (Tsushima et al. 2006). In the present case, the long-term temperature and ozone trends during this period are small and the

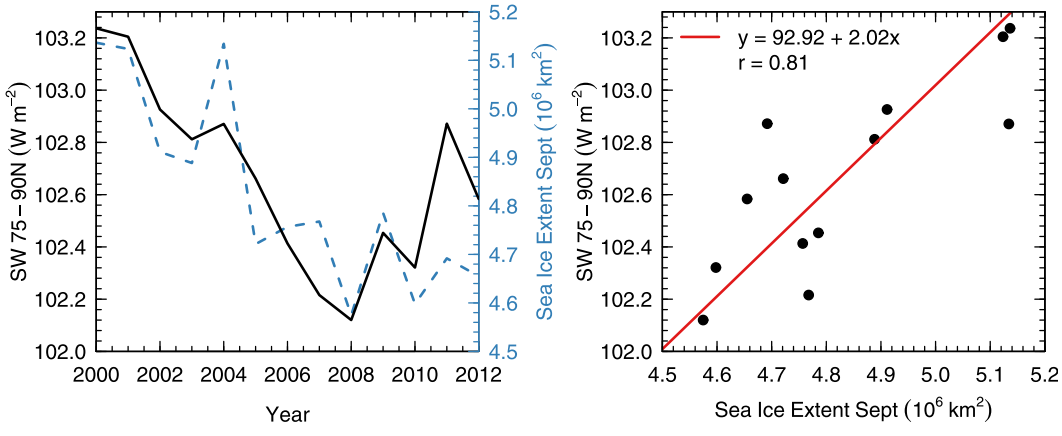


FIG. 5. As in Fig. 4, but for the multimodel mean of the CMIP5 model integrations.

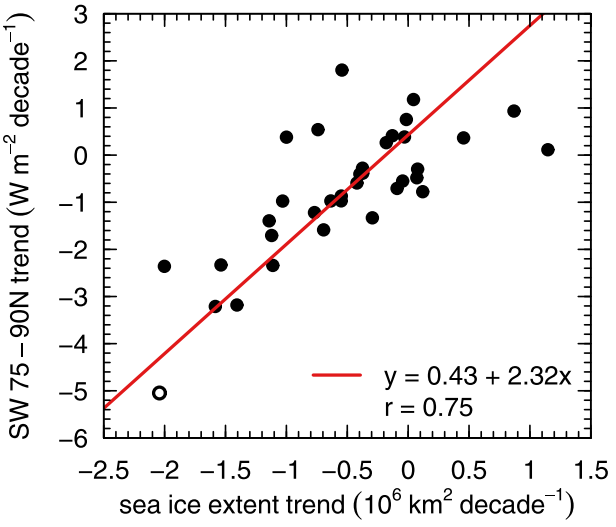


FIG. 6. Trend from 2000 to 2012 for 75°–90°N reflected shortwave vs same trend for sea ice extent. Solid circles indicate the trends calculated from 34 CMIP5 models. The open circle represents observations not included in the regression shown.

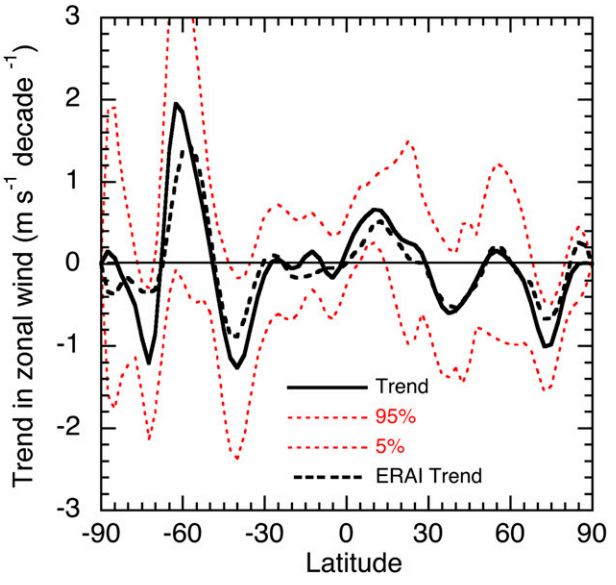


FIG. 7. As in Fig. 1, but for the trend of annual-mean zonal wind from NCEP–NCAR reanalysis averaged over the 700–300-hPa layer. The dashed line shows a comparable trend for ERA-Interim.

trend we see is most likely to be associated with natural variability, possibly because of the trend toward La Niña conditions.

To show the relationship of the SW trend to circulation changes, we compute the trends of meteorological fields over the Southern Hemisphere and see that they reflect a change in meteorology that can be logically associated with the shortwave trends. Figure 7 shows the trend in zonal wind averaged over the 700–300-hPa layer in the same format as Fig. 1. Statistically significant trends occur over the Southern Ocean, with increasing winds in the band from 45° to 65°S and decreasing winds to the north and south of that. Trends are shown for both NCEP–NCAR and ERA-Interim reanalyses to demonstrate that these trends are not very sensitive to the dataset used, although the ERA-Interim trend is smaller. The wind increases by about 2 m s^{-1}, while the SW increases by about 2 W m^{-2}, giving a simple one-to-one scaling of the annual-mean wind increase with the SW increase of 1 W m^{-2} (m s^{-1})$^{-1}$ of wind increase. The relationship of cloud shortwave reflection to a poleward wind shift, with increased solar reflection poleward of the jet and decreased solar reflection equatorward of it, may help to enhance or sustain the poleward movement of the jet, since cloud radiative effects influence the latitude of the jet in CMIP5 simulations (Ceppi et al. 2012).

While the SW trend signal is strongest in Southern Hemisphere (SH) summer because of the seasonal variation of insolation, the wind trend signature shows no strong seasonal preference, with the westerly intensification trend over the Southern Ocean apparent in every season (not shown). In this time period the zonal wind over the Southern Ocean in summer is somewhat correlated with the zonal wind during the previous winter. A statistically significant reduction in zonal winds is also seen near 70°N, which comes primarily from the Northern Hemisphere (NH) spring and summer season and may be related to the ice melt in the Arctic (Ogi and Wallace 2012; Screen et al. 2013). A westerly trend is also apparent around 15°N and is likely related to the La Niña trend, which concentrates more convective heating and Rossby wave driving north of the equator.

As an index of southern annular mode variability we have considered the Antarctic Oscillation index (AAO) as well as zonal averages of zonal wind averaged over 700–300 hPa between 45° and 65°S. These two indices are correlated with each other at 0.95. For the tropospheric wind index we hereafter use the ERA-Interim zonal winds averaged over 300–700 hPa and area averaged over 45°–65°S.

Despite the strongly suggestive temporal trends of SW and zonal wind in the band from 45° to 65°S it appears that the robust linear trend in SW is more strongly connected to Antarctic sea ice than to the zonal winds. Satellite data indicate that sea ice concentration around Antarctica has been increasing (Cavalieri and Parkinson 2008; Comiso and Nishio 2008; Parkinson and Cavalieri 2012; Screen 2011). The increase in sea ice concentration in the band from 55° to 65°S appears to be a substantial contributor to the increase in shortwave reflection over the period from 2000 to 2012 for which

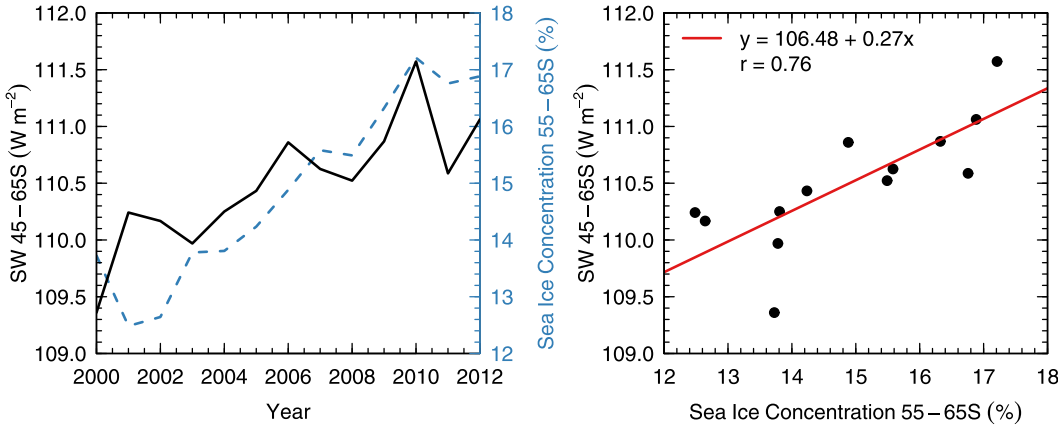


FIG. 8. Observed annual mean of SW averaged from 45° to 65°S and sea ice concentration averaged from 55° to 65°S (left) plotted vs year from 2000 to 2012 and (right) as a scatterplot.

we have CERES observations. Figure 8 shows the annual-mean reflected shortwave and sea ice concentration, which both have increasing trends over this period. Sea ice concentrations also increase poleward of 65°S, but we limit consideration to 55°–65°S since this includes all the sea ice variations within the band where the SW increases with time. The trend in sea ice is a major contributor to the trend in SW in the band from 45° to 65°S during the period, but the trend in SW extends beyond the region that is directly influenced by sea ice (Figs. 1–3).

Table 1 shows the correlation matrix between various indices that are likely involved in the trends observed. For a sample size of 13 annual means, the 5% and 95% confidence limits on correlation are ±0.48, using a null hypothesis that the true correlation is zero. We have chosen the band from 45° to 65°S for SW and winds, since these are where the records show significant trends and also because these latitudes correspond to the poleward lobe of wind variations associated with the southern annular mode (e.g., Hartmann and Lo 1998). Table 1 indicates strong correlations of SW with sea ice concentration and also significant correlations with tropospheric wind. The correlation with wind is still significant if the temporal trend is first removed from the data. Also shown is that stratospheric winds are significantly correlated with tropospheric winds, and Niño-3.4 is significantly correlated with both tropospheric and stratospheric winds. The connection between tropospheric and stratospheric annular variability is well established for both hemispheres (Thompson and Wallace 2000). L'Heureux and Thompson (2006) found that about 25% of the Southern Hemisphere annular variability was related to ENSO. The connection of the annular variability to ENSO in the Southern Hemisphere has recently been discussed by Lin et al. (2012), who showed that the stationary wave variability in the extratropics increases during La Niña conditions, mostly through the meridional propagation in the troposphere. The stationary wave variability then establishes a link to the stratosphere. The mechanisms are increasingly better understood whereby the Hadley cell expands during La Niña (Seager et al. 2003) and the extratropical eddy-driven jet shifts north and south with the Hadley cell edge (Kang and Polvani 2011; Ceppi and Hartmann 2013). It is therefore expected that the midlatitude westerly jet in the troposphere and stratosphere would be shifted poleward and intensified by La Niña conditions.

Figure 9 shows the trend of the 700–300-hPa zonal wind in the CMIP5 models during 1970–2012, along with the trend in observed wind repeated from Fig. 7. The observed wind trend is much stronger, primarily because the natural variability in 2000–12 trended strongly toward a positive annular mode during this period. Figure 9 also shows the trend in shortwave in the models along with a rescaling of the shortwave trend to estimate what the

TABLE 1. Correlation matrix for annual-mean values of some selected indices. Tropospheric wind (*U* Trop) is averaged over 300–700 hPa and stratospheric wind (*U* Strat) is for 10 hPa. All latitude bands are area-weighted averages. Correlations larger than 0.48 are considered significant (see text).

	SW 45°–65°S	Sea ice 55°–65°S	*U* Trop 45°–65°S	*U* Strat 45°–65°S	Niño-3.4
SW 45°–65°S	1				
Sea ice 55°–65°S	0.76	1			
U Trop 45°–65°S	0.51	0.40	1		
U Strat 45°–65°S	0.29	0.35	0.63	1	
Niño-3.4	−0.13	−0.40	−0.53	−0.55	1

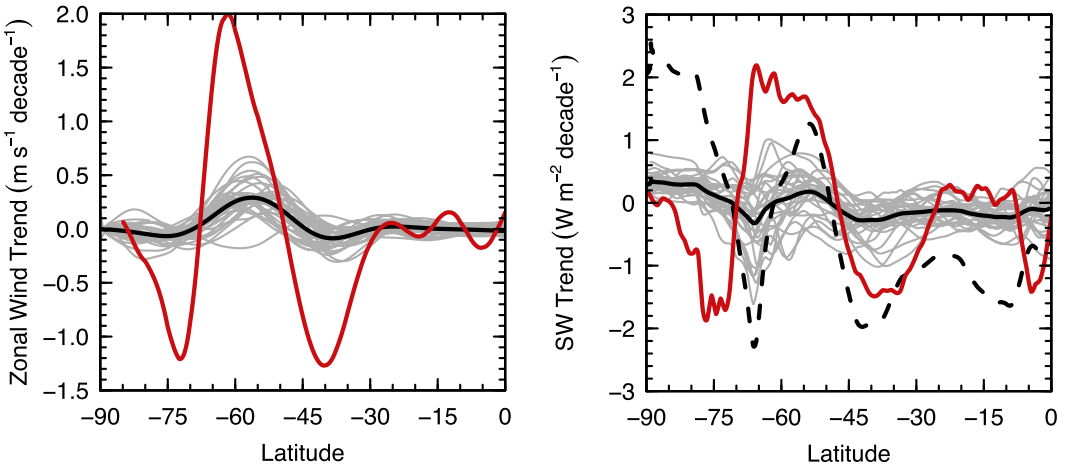


FIG. 9. Comparison of the observed annual-mean trends during 2000–12 (red line) and from CMIP5 models over the 1970–2012 period (gray lines) for (left) zonal-mean wind averaged for 700–300 hPa and (right) the SW trend. The black line represents the multimodel mean, and the dashed line represents the model means rescaled to the observed zonal wind change at 60°S.

model shortwave trend would be if the multimodel-mean wind shift was as large as the NCEP–NCAR change in the left panel. The rescaled model shortwave trends agree with the observations between 30° and 50°S but depart significantly from observations outside this interval. The models produce a significant hemispherically integrated net reduction in reflected shortwave in association with a poleward shift of the jet, whereas we will see in section 3d that the observed changes in reflected solar radiation tend to integrate to a smaller number, although the observed trend in SW at higher latitudes has contributions from sea ice change that are not included in the model results. Of course the CMIP5 simulated changes over 1970–2012 are likely driven by different mechanisms than drive the mostly natural interannual variability in the observed trends over 2000–12. For global warming it might be expected that the declining sea ice trends in the Antarctic would be opposite to the increasing Antarctic sea ice observed in 2000–12, and this explains much of the discrepancy between CMIP5 models and the observations between 55° and 70°S in Fig. 9.

As a further comparison with models we show in Fig. 10 the trend in SW over 2000–08 from the AMIP simulations from the CMIP5 archive, along with the trend in sea ice concentration from the merged Hadley Centre–NOAA OI dataset and the SW trend from CERES over the same period. The CMIP5 AMIP archive stops in 2008, so we compare for the shorter period in which CERES and AMIP overlap. The regions of best agreement for SW between AMIP and observations are in the polar regions, where the observed sea ice concentrations were used to force the AMIP models. Some of the tropical signature associated with ENSO is also captured, but the trends in SW over the Southern Ocean midlatitudes that appear to be associated with annular mode variations are not captured by the AMIP simulations. It is tempting to conclude that the models are not capturing the SW response to ENSO in the extratropics, but the record is short and the level of natural variability of the southern annular mode is large.

Figure 11 shows the trend of zonal-mean OLR over the 2000–12 period as a function of latitude. In high southern latitudes it has a similar shape to the year-to-year variability and its structure is consistent with a poleward jet shift and intensification. The most significant features are an increase of OLR over the Arctic,

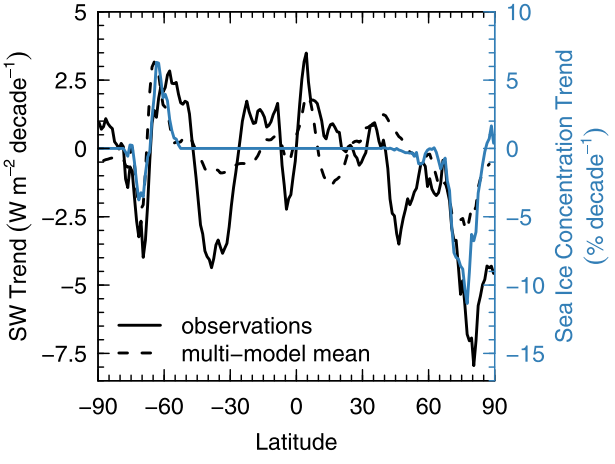


FIG. 10. Trends over the 2000–08 period for SW in AMIP models (dashed), SW from CERES (solid), and sea ice concentration from the merged Hadley Centre–NOAA OI dataset (blue). All are based on annual-mean data.

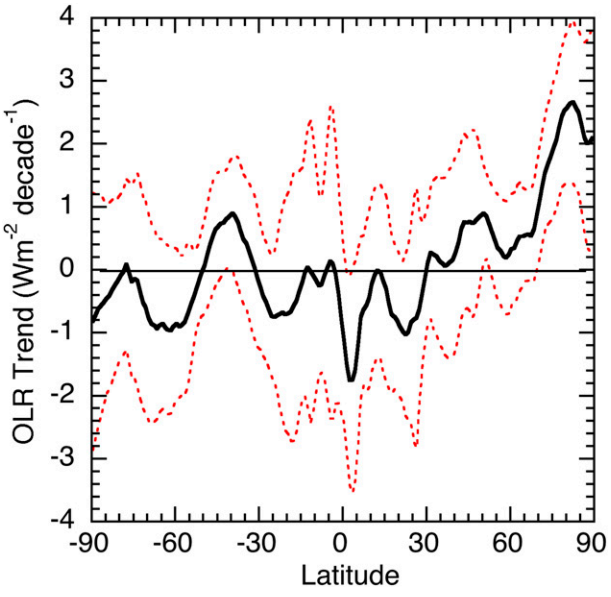


FIG. 11. As in Fig. 1, but for OLR.

which we can associate with ice melting, and a decrease just north of the equator in association with the El Niño trend over this period. The outgoing longwave radiation (OLR) shows a much more robust connection to the annular mode variability than the SW. The correlation between OLR over 60°–90°S and tropospheric zonal wind over 45°–65°S is 0.91. This high correlation is because the jet shift has a strong signature in the temperature field, via the thermal wind relationship. As the jet shifts poleward and simultaneously intensifies, the air becomes cooler poleward of the jet and the OLR decreases with this cooling. Cloud changes may also contribute to the change in OLR, but this contribution is likely of the same sign and smaller than the effect of temperature. The air cools by sinking less, which might be expected to give an increase in high clouds, further contributing to the reduction in OLR but probably marginally so compared to the direct temperature effect. The cloud reflectivity depends less sensitively on the zonal jet structure, since the dominant cloud type for reflection is low cloud. Low clouds are in large part driven by the vertical exchange of energy in the boundary layer, so they are less directly linked to zonal wind shifts than temperature and OLR. Figure 12 shows a close relationship between the annual-mean tropospheric wind at 45°–65°S and the OLR averaged over the area of the polar cap from 60° to 90°S. This signature is slightly stronger in the winter season (not shown).

d. *Area averages and northward transports*

To quantify how the trends in shortwave reflection affect larger areas, we integrate the trends in Fig. 1 over the north and south polar caps as in (1), where φ is latitude and $x = \sin\varphi$. The term $S^{\uparrow}$ represents the trend in SW,

$$F_{\mathrm{SP}}(\varphi) = \frac{\int_{-1}^{\sin\varphi} S^{\uparrow}\, dx}{\int_{-1}^{\sin\varphi} dx} \quad \text{and} \quad F_{\mathrm{NP}}(\varphi) = \frac{\int_{\sin\varphi}^{1} S^{\uparrow}\, dx}{\int_{\sin\varphi}^{1} dx}. \qquad (1)$$

These integrals as functions of latitude are shown in Fig. 13. Following the south polar cap integral (blue line), one can see that the contributions to increased reflection in the 45°–65°S band are very nearly canceled by the trends of opposite sign in the 20°–45°S band, so that not much net change results from the Southern Ocean trends,

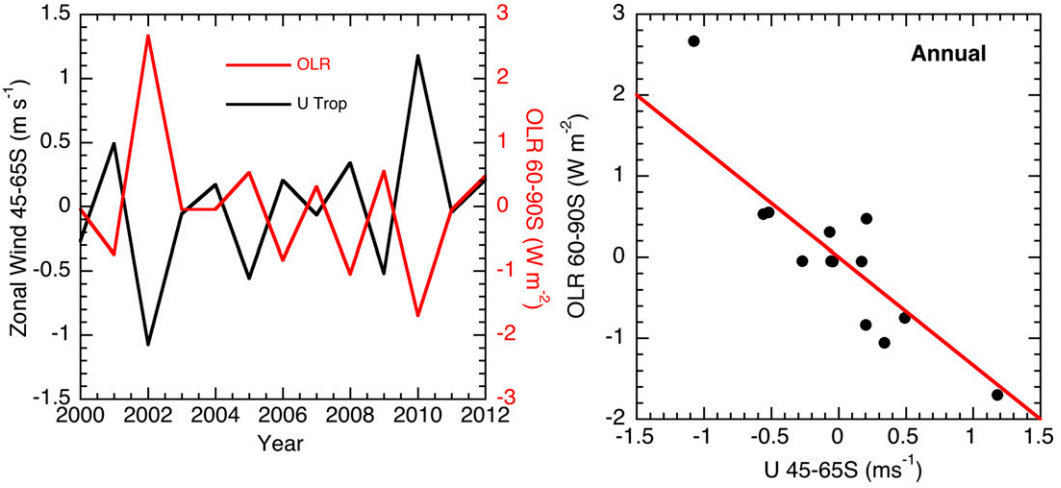


FIG. 12. (left) OLR averaged for the region 60°–90°S and the tropospheric wind index for 45°–65°S annual-average anomalies vs year and (right) scatterplot of the same quantities with the linear fit ($R = 0.91$).

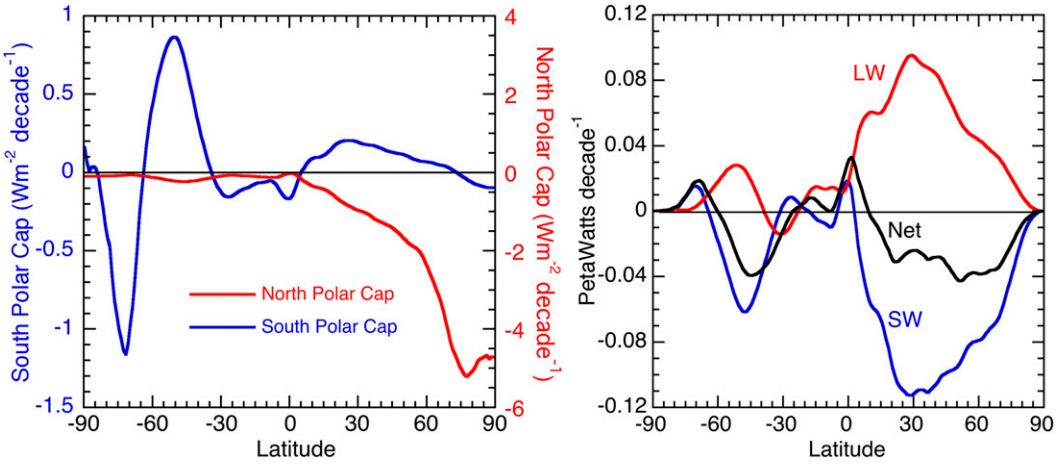


FIG. 13. (left) Integrals of reflected solar radiation trends over the southern and northern polar caps as functions of latitude and (right) trends of northward energy flux implied by the trends in top-of-atmosphere energy flux.

which are associated partly with sea ice concentration increases and partly with the cloud response to a jet shift. The trend in global-mean reflected solar radiation is most easily read from the south polar cap integral at the North Pole and is about $-0.1\,\mathrm{W\,m^{-2}}$. The area average of the integral of SW trend over the south polar cap reaches a maximum of $+0.86\,\mathrm{W\,m^{-2}\,decade^{-1}}$ at 50°S, which implies an increase in the required poleward energy flux of about 0.06 PW or about 1% of the total poleward flux. The area-average SW trend poleward of 34°S is zero and reaches a maximum negative value (increased solar absorption) of $-0.16\,\mathrm{W\,m^{-2}\,decade^{-1}}$ at 27°S, indicating a rather small net energy gain in the Southern Hemisphere. A significant difference between the observed south polar cap integral and the equivalent calculation for the rescaled model response in Fig. 9 is the weakness of the increased reflection between 45° and 65°S in the models. In consequence of this, the model integral is about $-0.6\,\mathrm{W\,m^{-2}}$ at 30°S, where the observational integral is only $-0.1\,\mathrm{W\,m^{-2}\,decade^{-1}}$. A significant portion of this difference is related to the increase in sea ice concentration in high southern latitudes, which does not occur in the simulations.

Polvani and Smith (2013) suggest that the Antarctic sea ice trends are within the range expected from natural variability exhibited by CMIP5 simulations. Sea ice variations are known to occur in conjunction with the annular mode. In both the long-term trend (Parkinson and Cavalieri 2012) and in the response to the southern annular mode and ENSO (Lefebvre et al. 2004; Liu et al. 2004; Simpkins et al. 2012), changes of opposite sign tend to occur in the Ross Sea area and the Bellingshausen/Amundsen Seas area. Modeling suggests that the asymmetries in the sea ice response can be explained by asymmetries in the mechanical and thermal forcing of sea ice by annular mode variability (Lefebvre and Goosse 2005; Sen Gupta and England 2006; Turner et al. 2009). The sea ice trends over the 2000–12 period are more zonally symmetric (not shown). Lefebvre and Goosse (2008) argue that during winter each Antarctic sea ice sector changes independently.

For the north polar cap integral (red line in left panel of Fig. 4) the polar cap area average is initially quite large ($-6\,\mathrm{W\,m^{-2}}$) and gradually decreases to near zero at the equator. Note that the scales for the two hemispheres are quite different. As one proceeds south across the equator, trends in southern midlatitudes cause a small reduction in global reflection from 20° to 45°S, which is then erased by the trends in the 45°–65°S band, indicating the energetic significance of the high-latitude sea ice and cloud brightening.

The right panel in Fig. 13 shows the changes in the implied northward energy flux from the trends in shortwave, longwave, and net radiation, assuming that the northward flux balances the trends at the top of the atmosphere. The global mean of $-0.1\,\mathrm{W\,m^{-2}\,decade^{-1}}$ was removed prior to this calculation. The reduction in northward flux implied by the shortwave trends is offset by trends in longwave emission, so that the reduction in flux implied by the net radiation is considerably less. Although the gradient in flux is largest over the Arctic region where the decreases in SW are greatest, the flux anomalies continue to increase all the way to 30°N. The extension to lower latitudes is contributed by the small reductions of SW in the midlatitudes, whose genesis is unclear to us. In the Southern Hemisphere the compensation between SW and longwave trends is less, so that the increase in poleward flux is of the same magnitude as in the Northern Hemisphere, though

the changes in shortwave flux are smaller in the Southern Hemisphere.

4. Summary and discussion

The 13-yr record of CERES earth radiation budget measurements, although relatively short for climate purposes, reveals three statistically significant linear trends of annual means over the 2000–12 period. These are related to 1) the declining Arctic sea ice, 2) increasing sea ice concentrations and shifting of the zonal wind pattern over the Southern Ocean, and 3) ENSO variability. Based on the linear trend of annual means, we estimate that a reduction in September Arctic sea ice extent of 10^6 km^2 results in an increase in solar absorption over the polar cap from 75° to 90°N of 2.5 W m^{-2} or an albedo decrease of about 0.013. Although sea ice trends in the CMIP5 model ensemble are much smaller than observed during the interval 2000–12, the relationship between sea ice decline and reflected solar radiation is similar, indicating that ice albedo changes and their relationship with cloud albedo are reasonably treated in the models.

CERES and reanalysis data from 2000 to 2012 indicate that, for annual means, increasing upper-level zonal winds in the latitude band from 45° to 65°S by 1 m s^{-1} result in an increase in shortwave reflection of about 1 W m^{-2} in the same band, but a significant portion of the increased reflection is associated with increasing Antarctic sea ice during this period. Decreases in reflected radiation occur in other latitudes, however, such that the hemispheric-average shortwave reflection is virtually unchanged. While models capture some of the trends associated with annular mode variability in the Southern Hemisphere, the increased reflectivity in high latitudes associated with sea ice is not a feature of CMIP5 global warming simulations. They simulate reduced reflection equatorward of 45°S of about the observed magnitude but produce much less brightening poleward of 55°S than is observed during the 2000–12 period.

Grise et al. (2013, hereafter G13) presented radiation budget changes associated with the positive (poleward) shift of the southern annular mode (SAM) index in simulations with the CAM3 model and compare with ISCCP cloud changes. The pattern of response they obtain is quite different than the trend in Fig. 1 and gives a much stronger impact on the hemispheric energy balance. They find a decrease of cloud reflection across 35°–60°S and an increase in reflection from 15° to 35°S, whereas the trend in Fig. 1 is an increase of reflection from 45° to 70°S and a decrease from 25° to 45°S, so that these structures are nearly orthogonal to each other. G13 considered the December–February season, whereas Fig. 1 shows the annual mean. We find that the structure of the trend for the December–February mean is similar to the annual mean in Fig. 1, with slightly larger trends and greater uncertainty. If we regress the zonal-mean SW onto the 45°–65°S wind index we have used here, the regressions for the annual mean and December–January mean are quite noisy but do show a brightening of clouds in the 45°–65°S band similar to the trend. The noisy relationship between indices of the annular mode and the CERES SW indicates that the annular mode is not a dominant influence on the zonal-mean SW during this period. If we regress the zonal winds and SW in the CMIP5 models against an index of the southern annular mode, the multimodel mean shows a reduction of cloud reflection equatorward of the jet but no substantial increase poleward of the jet, in basic agreement with the analysis of G13 (not shown).

In contrast, the trend of OLR found here is in good agreement with the structure found by G13 and in the regressions of the multimodel CMIP5 simulations, with a reduction of OLR poleward of about 50°S and an increase around 30°–45°S, which appear to follow the temperature changes required by thermal wind. This suggests that the structure of the large-scale dynamical shift is similar in the observations shown here, in G13 and in CMIP5, but that the shift in shortwave reflection is very different. This would be consistent with the great diversity of climate model responses in Fig. 9 and with the general wisdom that cloud shortwave responses are uncertain and vary greatly from model to model (e.g., Ceppi et al. 2012).

An assessment of the robustness of the trends seen in the 2000–13 period is difficult without a longer dataset. Since the period of record is short and the trends in wind and SW in the Southern Hemisphere seem to be influenced in part by ENSO changes and in part by as yet unexplained increases in sea ice concentration, it would be dangerous to assume that the relationships found here would apply to climate change or other forms of annular variability. In particular, it is not certain that the data presented here give a robust estimate of what cloud responses we should expect from a shift in the southern annular mode, since sea ice and other things are changing at the same time.

Acknowledgments. The authors thank Kevin Grise, Norman Loeb, Angie Pendergrass, and an anonymous reviewer for helpful suggestions. The CERES data were obtained from the NASA Langley Research Center Atmospheric Science Data Center. Reanalysis data were obtained from NOAA and ECMWF web resources. The authors were supported by NSF Grant AGS-0960497 and NASA Grant NNX09AH73G.

APPENDIX

CMIP5 models used in the analysis

A list of the 34 CMIP5 models analyzed, their expanded names, and the institutions responsible for the models are in Table A1.

TABLE A1. List of CMIP5 models used in the analysis.

Model acronym	Expanded model name	Institute
ACCESS1.0	Australian Community Climate and Earth-System Simulator, version 1.0	Commonwealth Scientific and Industrial Research Organisation (CSIRO)–Bureau of Meteorology (BOM)
ACCESS1.3	Australian Community Climate and Earth-System Simulator, version 1.3	CSIRO–BOM
BCC-CSM1.1	Beijing Climate Center, Climate System Model, version 1.1	Beijing Climate Center (BCC)
BCC-CSM1.1(m)	Beijing Climate Center, Climate System Model, version 1.1(m)	BCC
BNU-ESM	Beijing Normal University–Earth System Model	College of Global Change and Earth System Science (GCESS), Beijing Normal University
CanESM2	Second Generation Canadian Earth System Model	Canadian Centre for Climate Modelling and Analysis (CCCma)
CCSM4	Community Climate System Model, version 4	NCAR
CESM1 (BGC)	Community Earth System Model, version 1 (Biogeochemistry)	National Science Foundation (NSF)–U.S. Department of Energy (DOE)–NCAR
CESM1 (CAM5)	Community Earth System Model, version 1 (Community Atmosphere Model, version 5)	NSF–DOE–NCAR
CMCC-CESM	Centro Euro-Mediterraneo per I Cambiamenti Climatici Carbon Earth System Model	Centro Euro-Mediterraneo per I Cambiamenti Climatici (CMCC)
CMCC-CM	Centro Euro-Mediterraneo per I Cambiamenti Climatici Climate Model	CMCC
CNRM-CM5	Centre National de Recherches Météorologiques Coupled Global Climate Model, version 5	Centre National de Recherches Météorologiques (CNRM)–Centre Européen de Recherche et de Formation Avancée en Calcul Scientifique (CERFACS)
CSIRO Mk3.6.0	Commonwealth Scientific and Industrial Research Organisation Mark, version 3.6.0	CSIRO– Queensland Climate Change Centre of Excellence (QCCCE)
FGOALS-g2	Flexible Global Ocean–Atmosphere–Land System Model gridpoint, version 2	State Key Laboratory of Numerical Modeling for Atmospheric Sciences and Geophysical Fluid Dynamics (LASG)–Center for Earth System Science (CESS)
GFDL CM3	Geophysical Fluid Dynamics Laboratory Climate Model, version 3	NOAA/Geophysical Fluid Dynamics Laboratory (GFDL)
GFDL-ESM2G	Geophysical Fluid Dynamics Laboratory Earth System Model with Generalized Ocean Layer Dynamics component	NOAA/GFDL
GFDL-ESM2M	Geophysical Fluid Dynamics Laboratory Earth System Model with Modular Ocean Model 4 component	NOAA/GFDL
GISS-E2H	Goddard Institute for Space Studies Model E2, coupled with the Hybrid Coordinate Ocean Model (HYCOM)	National Aeronautics and Space Administration (NASA) Goddard Institute for Space Studies (GISS)
GISS-E2-R	Goddard Institute for Space Studies Model E2, coupled with the Russell ocean model	NASA GISS
HadGEM2-AO	Hadley Centre Global Environment Model, version 2–Atmosphere and Ocean	National Institute of Meteorological Research (NIMR), Korea Meteorological Administration (KMA)
HadGEM2-CC	Hadley Centre Global Environment Model, version 2–Carbon Cycle	Met Office (UKMO) Hadley Centre
HadGEM2-ES	Hadley Centre Global Environment Model, version 2–Earth System	UKMO Hadley Centre

TABLE A1. (*Continued*)

Model acronym	Expanded model name	Institute
INM-CM4.0	Institute of Numerical Mathematics Coupled Model, version 4.0	Institute of Numerical Mathematics (INM)
IPSL-CM5A-LR	L'Institut Pierre-Simon Laplace Coupled Model, version 5A, coupled with Nucleus for European Modelling of the Ocean (NEMO), low resolution	L'Institut Pierre-Simon Laplace (IPSL)
IPSL-CM5A-MR	L'Institut Pierre-Simon Laplace Coupled Model, version 5A, coupled with NEMO, mid resolution	IPSL
IPSL-CM5B-LR	L'Institut Pierre-Simon Laplace Coupled Model, version 5B, coupled with NEMO, low resolution	IPSL
MIROC5	Model for Interdisciplinary Research on Climate, version 5	Model for Interdisciplinary Research on Climate (MIROC)
MIROC-ESM	Model for Interdisciplinary Research on Climate, Earth System Model	MIROC
MIROC-ESM-CHEM	Model for Interdisciplinary Research on Climate, Earth System Model, Chemistry Coupled	MIROC
MPI-ESM-LR	Max Planck Institute Earth System Model, low resolution	Max Planck Institute for Meteorology (MPI-M)
MPI-ESM-MR	Max Planck Institute Earth System Model, medium resolution	MPI-M
MRI-CGCM3	Meteorological Research Institute Coupled Atmosphere–Ocean General Circulation Model, version 3	Meteorological Research Institute (MRI)
NorESM1-M	Norwegian Earth System Model, version 1 (intermediate resolution)	Norwegian Climate Centre (NCC)
NorESM1-ME	Norwegian Earth System Model, version 1 (intermediate resolution with carbon cycle)	NCC

REFERENCES

Barnes, E. A., and D. L. Hartmann, 2010: Testing a theory for the effect of latitude on the persistence of eddy-driven jets using CMIP3 simulations. *Geophys. Res. Lett.,* **37,** L15801, doi:10.1029/2010GL044144.

Bender, F. A. M., V. Ramanathan, and G. Tselioudis, 2012: Changes in extratropical storm track cloudiness 1983–2008: Observational support for a poleward shift. *Climate Dyn.,* **38,** 2037–2053.

Bretherton, C. S., M. Widmann, V. P. Dymnikov, J. M. Wallace, and I. Blade, 1999: The effective number of spatial degrees of freedom of a time-varying field. *J. Climate,* **12,** 1990–2009.

Cavalieri, D. J., and C. L. Parkinson, 2008: Antarctic sea ice variability and trends, 1979–2006. *J. Geophys. Res.,* **113,** C07004, doi:10.1029/2007JC004564.

Ceppi, P., and D. L. Hartmann, 2013: On the speed of the eddy-driven jet and the width of the Hadley cell in the Southern Hemisphere. *J. Climate,* **26,** 3450–3465.

——, Y. T. Hwang, D. M. W. Frierson, and D. L. Hartmann, 2012: Southern Hemisphere jet latitude biases in CMIP5 models linked to shortwave cloud forcing. *Geophys. Res. Lett.,* **39,** L19708, doi:10.1029/2012GL053115.

Chiang, J. C. H., and C. M. Bitz, 2005: Influence of high latitude ice cover on the marine intertropical convergence zone. *Climate Dyn.,* **25,** 477–496.

Comiso, J. C., and F. Nishio, 2008: Trends in the sea ice cover using enhanced and compatible AMSR-E, SSM/I, and SMMR data. *J. Geophys. Res.,* **113,** C02S07 doi:10.1029/2007JC004257.

Dee, D. P., and Coauthors, 2011: The ERA-Interim reanalysis: Configuration and performance of the data assimilation system. *Quart. J. Roy. Meteor. Soc.,* **137,** 553–597.

Derksen, C., and R. Brown, 2012: Spring snow cover extent reductions in the 2008–2012 period exceeding climate model projections. *Geophys. Res. Lett.,* **39,** L19504, doi:10.1029/2012GL053387.

Fetterer, F., K. Knowles, W. Meier, and M. Savoie, cited 2009: Sea ice index. National Snow and Ice Data Center, Boulder, CO, digital media. [Available online at http://nsidc.org/data/docs/noaa/g02135_seaice_index/.]

Flanner, M. G., K. M. Shell, M. Barlage, D. K. Perovich, and M. A. Tschudi, 2011: Radiative forcing and albedo feedback from the Northern Hemisphere cryosphere between 1979 and 2008. *Nat. Geosci.,* **4,** 151–155.

Frierson, D. M. W., and Y. T. Hwang, 2012: Extratropical influence on ITCZ shifts in slab ocean simulations of global warming. *J. Climate,* **25,** 720–733.

Grise, K. M., L. M. Polvani, G. Tselioudis, Y. Wu, and M. D. Zelinka, 2013: The ozone hole indirect effect: Cloud-radiative anomalies accompanying the poleward shift of the eddy-driven jet in the Southern Hemisphere. *Geophys. Res. Lett.,* **40,** 3688–3692, doi:10.1002/GRL.50675.

Hartmann, D. L., and F. Lo, 1998: Wave-driven zonal flow vacillation in the Southern Hemisphere. *J. Atmos. Sci.,* **55,** 1303–1315.

Hurrell, J. W., J. J. Hack, D. Shea, J. M. Caron, and J. Rosinski, 2008: A new sea surface temperature and sea ice boundary dataset for the Community Atmosphere Model. *J. Climate,* **21,** 5145–5153.

Kalnay, E., and Coauthors, 1996: The NCEP/NCAR 40-Year Reanalysis Project. *Bull. Amer. Meteor. Soc.,* **77,** 437–471.

Kang, S. M., and L. M. Polvani, 2011: The interannual relationship between the latitude of the eddy-driven jet and the edge of the Hadley cell. *J. Climate,* **24,** 563–568.

Kay, J. E., and A. Gettelman, 2009: Cloud influence on and response to seasonal Arctic sea ice loss. *J. Geophys. Res.,* **114,** D18204, doi:10.1029/2009JD011773.

Kushner, P. J., I. M. Held, and T. L. Delworth, 2001: Southern Hemisphere atmospheric circulation response to global warming. *J. Climate,* **14,** 2238–2249.

Lefebvre, W., and H. Goosse, 2005: Influence of the southern annular mode on the sea ice-ocean system: The role of the thermal and mechanical forcing. *Ocean Sci.,* **1,** 145–157.

——, and ——, 2008: An analysis of the atmospheric processes driving the large-scale winter sea ice variability in the Southern Ocean. *J. Geophys. Res.,* **113,** C02004, doi:10.1029/2006JC004032.

——, ——, R. Timmermann, and T. Fichefet, 2004: Influence of the southern annular mode on the sea ice–ocean system. *J. Geophys. Res.,* **109,** C09005, doi:10.1029/2004JC002403.

L'Heureux, M. L., and D. W. J. Thompson, 2006: Observed relationships between the El Niño–Southern Oscillation and the extratropical zonal-mean circulation. *J. Climate,* **19,** 276–287.

Lin, P., Q. Fu, and D. L. Hartmann, 2012: Impact of tropical SST on stratospheric planetary waves in the Southern Hemisphere. *J. Climate,* **25,** 5030–5046.

Liu, J. P., J. A. Curry, and D. G. Martinson, 2004: Interpretation of recent Antarctic sea ice variability. *Geophys. Res. Lett.,* **31,** L02205, doi:10.1029/2003GL018732.

Loeb, N. G., S. Kato, W. Su, T. Wong, F. G. Rose, D. R. Doelling, J. R. Norris, and X. Huang, 2012a: Advances in understanding top-of-atmosphere radiation variability from satellite observations. *Surv. Geophys.,* **33,** 359–385.

——, J. M. Lyman, G. C. Johnson, R. P. Allan, D. R. Doelling, T. Wong, B. J. Soden, and G. L. Stephens, 2012b: Observed changes in top-of-the-atmosphere radiation and upper-ocean heating consistent within uncertainty. *Nat. Geosci.,* **5,** 110–113.

Ogi, M., and J. M. Wallace, 2012: The role of summer surface wind anomalies in the summer Arctic sea ice extent in 2010 and 2011. *Geophys. Res. Lett.,* **39,** L09704, doi:10.1029/2012GL051330.

Parkinson, C. L., and D. J. Cavalieri, 2012: Antarctic sea ice variability and trends, 1979-2010. *Cryosphere,* **6,** 871–880.

Polvani, L. M., and K. L. Smith, 2013: Can natural variability explain observed Antarctic sea ice trends? New modeling evidence from CMIP5. *Geophys. Res. Lett.,* **40,** 3195–3199, doi:10.1002/grl.50578.

Rayner, N. A., D. E. Parker, E. B. Horton, C. K. Folland, L. V. Alexander, D. P. Rowell, E. C. Kent, and A. Kaplan, 2003: Global analyses of sea surface temperature, sea ice, and night marine air temperature since the late nineteenth century. *J. Geophys. Res.,* **108,** 4407, doi:10.1029/2002JD002670.

Santer, B. D., and Coauthors, 2008: Consistency of modelled and observed temperature trends in the tropical troposphere. *Int. J. Climatol.,* **28,** 1703–1722.

Screen, J. A., 2011: Sudden increase in Antarctic sea ice: Fact or artifact? *Geophys. Res. Lett.,* **38,** L13702 doi:10.1029/2011GL047553.

——, I. Simmonds, C. Deser, and R. Tomas, 2013: The atmospheric response to three decades of observed Arctic sea ice loss. *J. Climate,* **26,** 1230–1248.

Seager, R., N. Harnik, Y. Kushnir, W. Robinson, and J. Miller, 2003: Mechanisms of hemispherically symmetric climate variability. *J. Climate,* **16,** 2960–2978.

Sen Gupta, A., and M. H. England, 2006: Coupled ocean–atmosphere–ice response to variations in the southern annular mode. *J. Climate,* **19,** 4457–4486.

Simpkins, G. R., L. M. Ciasto, D. W. J. Thompson, and M. H. England, 2012: Seasonal relationships between large-scale climate variability and Antarctic sea ice concentration. *J. Climate,* **25,** 5451–5469.

Stroeve, J. C., V. Kattsov, A. Barrett, M. Serreze, T. Pavlova, M. Holland, and W. N. Meier, 2012: Trends in Arctic sea ice extent from CMIP5, CMIP3 and observations. *Geophys. Res. Lett.,* **39,** L16502, doi:10.1029/2012GL052676.

Sveshnikov, A. A., 1968: *Problems in Probability Theory, Mathematical Statistics and Theory of Random Functions.* Dover, 481 pp.

Taylor, K. E., R. J. Stouffer, and G. A. Meehl, 2012: An overview of the CMIP5 and the experiment design. *Bull. Amer. Meteor. Soc.,* **93,** 485–498.

Thompson, D. W. J., and J. M. Wallace, 2000: Annular modes in the extratropical circulation. Part I: Month-to-month variability. *J. Climate,* **13,** 1000–1016.

Tsushima, Y., and Coauthors, 2006: Importance of the mixed-phase cloud distribution in the control climate for assessing the response of clouds to carbon dioxide increase: A multi-model study. *Climate Dyn.,* **27,** 113–126.

Turner, J., and Coauthors, 2009: Non-annular atmospheric circulation change induced by stratospheric ozone depletion and its role in the recent increase of Antarctic sea ice extent. *Geophys. Res. Lett.,* **36,** L08502, doi:10.1029/2009GL037524.

Wang, M. Y., and J. E. Overland, 2012: A sea ice free summer Arctic within 30 years: An update from CMIP5 models. *Geophys. Res. Lett.,* **39,** L18501, doi:10.1029/2012GL052868.

Wielicki, B. A., B. R. Barkstrom, E. F. Harrison, E. B. Lee III, G. L. Smith, and J. E. Cooper, 1996: Clouds and the Earth's Radiant Energy System (CERES): An Earth Observing System experiment. *Bull. Amer. Meteor. Soc.,* **77,** 853–868.

Yin, J. H., 2005: A consistent poleward shift of the storm tracks in simulations of 21st century climate. *Geophys. Res. Lett.,* **32,** L18701, doi:10.1029/2005GL023684.

Zelinka, M. D., and D. L. Hartmann, 2012: Climate feedbacks and their implications for poleward energy flux changes in a warming climate. *J. Climate,* **25,** 608–624.